System Design of Underwater Battery Power System for Marine and Offshore Industry

Cheng Siong Chin[a,b*], Junbo Jia[c], Joel Hay King Chiew[c], Wei Da Toh[c], Zuchang Gao[c], Caizhi Zhang[b*], John McCann[d]

[a] *Faculty of Science, Agriculture, and Engineering, Newcastle University in Singapore, Singapore 599493 (corresponding author:cheng.chin@ncl.ac.uk)*
[b]*School of Automotive Engineering; The State Key Laboratory of Mechanical Transmissions; Chongqing Automotive Collaborative Innovation Center, Chongqing University, Chongqing, China, 400044; czzhang@cqu.edu.cn*
[c]*School of Engineering, Clean Energy Research Centre, Temasek Polytechnic, 21 Tampines Avenue 1, 529757, Singapore (joelchk@tp.edu.sg, weida@tp.edu.sg, zuchang@tp.edu.sg, jiajunbo@tp.edu.sg)*
[d]*SMD Singapore Pte Ltd, 33 Ubi Avenue 3, #01-59 VERTEX, Singapore 408868 (john.mccann@smd.sg)*

Abstract

Application of battery power systems increases in the marine and offshore industry. Most applications target to reduce the energy consumptions when the battery power system is wholly or partially used. The hardware and software of the battery power system design for underwater application are described. The testing of the battery power system is successfully performed in a water tank at low temperature of 4 °C that mimics subsea operating condition where most remotely-operated vehicle (ROV) operates. The average variation of state-of-charge for the 12-cell is approximately 5 percent after active cell balancing. The battery management system is capable of estimating the state-of-charge and using the data to perform the active cell balancing on each cell with different imbalanced state-of-charge values of at least 30 percent.

Keywords: battery power system; Lithium Iron Phosphate; offshore industry; remotely-operated vehicle; state-of-charge; active cell balancing.

1. Introduction

With increasing global demand for energy, facilities such as drilling, oil rig and production platforms have become essential assets for marine and offshore companies. Any defect to these facilities will have significant adverse environmental and economic consequences. For example, British Petroleum (BP) Deepwater Horizon oil rig exploded and killed eleven peoples and caused widespread pollution in the Gulf of Mexico. A report released by BP [1] concludes that accident was caused by "a

complex and interlinked series of mechanical failures, human judgments, engineering design, operational implementation, and team interfaces." Underwater systems such as electric-propelled underwater robotic vehicles (URVs): remotely-operated vehicle (ROV) and autonomous vehicle (AUV) for various deepwater applications have become more relevant to inspect any damages to these offshore oil rig platforms. The URVs enable continuous and effective real-time monitoring in deep water where human divers are unable to reach. In the past few decades, these robotic systems have become more prevalent and reliable for harsh and remote environment. The requirements placed on the battery power systems on these robotic applications have also become more stringent and demanding. More power and endurance are required, and the batteries must be robust enough to cope with a broader range of environmental conditions such as in marine vessel [2-4], AUV[5] and wind turbine [6]. It is especially true of batteries for ROVs used for emergency power supply. However, the endurance for the power system is mainly limited by the energy density [7] in the underwater applications.

Lithium iron phosphate battery or LiFePO4 battery has become quite common for electric vehicles[8-9], smart grids[10-12] and lately for AUV applications [13-14]. However, the batteries are quite vulnerable to ambient or operating temperature variation and unforeseen overly charged or discharged resulting in shorter lifespan and poor performance. Hence, it is essential to include the ambient temperature variation on the state-of-charge (SOC) [15-16] estimation. The experimental works [17] to study the variation of temperature on a prismatic Li-ion phosphate (LiFePO4) battery during the discharge process was conducted. The increased discharge rate resulted in higher temperatures on the battery's surface except for lower discharge rates; the temperature was close to the ambient temperature.

Further works to perform thermal characterization of thermo-physical properties such as thermal resistance and conductivity of prismatic battery materials of the lithium-ion battery can be seen in [18]. The electrochemical–thermal analysis [19] of the LiFePO4 was performed. The results showed the reaction heat is the major heat source in LiFePO4 battery, and the large temperature gradient across the cell was caused by high contact resistance. The modeling of the thermal effect of the LiFePO4 battery was studied using COMSOL[20-22], It was quite popular in studying the heat transfer problem of the battery. A different study on using Boron Nitride coating [23] on Lithium-ion battery casing and

its heat transfer properties was studied. The results showed that the coating could improve the thermal management of the battery. Alternate method [24] to model the thermal and electrical behavior of a Lithium-ion cell that reduced computation time was also proposed. The reviews of different approaches in modeling the Lithium-ion battery cell including thermal effect for land-based systems such as electric vehicles and smart grids can be found in the following references [25-29].

However, the marine-based LiFePO4 battery power module for underwater systems such as URV are rarely studied in the literature. There exist many different types of the marine-based battery power system in the market. The list of common types of battery used and the references [30-35] are tabulated in Table 1. The batteries for subsea are usually more rugged to withstand seawater ingress and subsea connectors that can tolerate high water pressure in URVs. As seen in Table 1, the energy capacity of the batteries has at least 1kWh, minimum static capacity of 18Ah and output current of 10 A. The mass of the battery can reach 90 kg. The battery cells are mainly: Lithium poly, Nickel–metal hydride battery, Lithium-ion, Lead-acid, Lead-carbon technology and Lithium–titanate. For marine applications (i.e. ship), they have higher charging and discharging current with larger form factor with fewer requirements on the enclosure design, connectors, and material as compared to batteries used for offshore in underwater applications. The marine battery power systems are often kept in a dry condition in battery room on board the ship. The common lead-acid batteries that the shipowner still use, can be quite heavy and space consuming when compared to Lithium-ion based battery.

Although, the battery power systems could be found in both marine and offshore industry, the process of developing, simulating to testing of the LiFePO4 battery power system for ROV in the offshore industry is not readily available in the literature. In this paper, the proposed Lithium-ion battery power system includes a smart battery management system (BMS) with active cell balancing technology, state of charge (SOC) and state of health (SOH) estimation. The proposed active cell balancing technology will transfer the energy from the most robust cell to the weakest cell and target to improve system efficiency as compared with passive cell balancing. It can lead to longer endurance in underwater and increase the battery lifespan for marine applications. Furthermore, the battery module with the BMS system can always be scalable (or can be stacked) to give a higher power capacity (up to 100kWh) for the underwater environment. The modular design of the battery allows user to quickly

swap a discharged battery with a charged one. It enables rapid turnaround of submersible equipment in the field. In addition, the battery power system comes with a pressure-resistance enclosure that eliminates extra battery pressure chamber and associated risk. Thus, increase system reliability amid high pressures down to 3000m of sea water that often limits most of the underwater activities.

This paper will focus on the development of a new 2 kWh (=50 Ah×3.2V×12 cells) Lithium Iron Phosphate (LiFePO4) battery power system for ROV that can be extended to power marine energy capture system and for energy storage purpose. The size of the battery power system is around 0.63 m long, and 0.44 m width with the mass in the air is approximately 98 kg. Therefore, the objectives of this paper are to design the mechanical and electrical subsystems, simulate the thermal behavior using COMSOL and test the functionality of the proposed LiFePO4 battery power system in the water tank.

The contributions made in this paper are as follows. A smart battery management system based on a micro-controller unit and digital signal processing technology is developed for ROV. The BMS consists of monitoring, protection and communication subsystems. It incorporates software algorithm of active cell balancing into a printed circuit board (PCB) for real-time testing with SOC estimation resulting in more balanced SOC value (of not more than 5% different) in water. A thermal simulation based on conjugate heat transfer module was performed on the battery power system in COMSOL, based on that, an underwater test station was first setup to simulate the battery power system in subsea environment of 4 °C.

Table 1: Different battery power system used in marine and offshore industry

Descriptions	**Bluefin's Robotics** [30]	**CDL subsea battery pack** [31]	**Southwest Electronic Energy Group (SWE)** [32]	**Deepsea Power & Light** [33]	**Furukawa Battery Company of Japan, Eco Marine Power** [34]	**PBES Lithium Industrial Batteries** [35]
Cell type	Lithium poly	Nickel–metal hydride battery	Lithium-ion	Lead-acid	Lead-Carbon Technology (FCP-1000-12)	Lithium–titanate (Titanate 35)
Dimensions (L x W x H)	384 x 133 x 210 mm	500x400x450mm	~1910x1890x650mm	457x305x327 mm	508 x 303 x 172 mm	580 x 320 x 380mm
Mass (Dry)	14.3 kg	46 kg	~75kg	49kg	75kg	90kg
Depth Rating	6,000 m	3000m	6000m	11,000m	NA	
Energy Capacity	1.5 kWh	0.95kWh	3.2kWh	NA	2kWh	3.5 kWh
Voltage (Nominal)	30 V	26.4V	29V	48V	2V	54V
Capacity (Nominal)	48 Ah	36Ah	112Ah	18Ah	1000Ah	60Ah
Discharge Current	10 A (nominal), 30 A (max)	NA	40 (nominal), 75 (max)	16A (max)	400A (max)	450A (max)
Discharge Temperature	-20 to 48 °C	NA	NA	-20°C to 60°C	5°C to 25°C	-40°C to +60°C
Charge Current	12 A (nominal), 15 A (max)	NA	29 A (nominal),32 A (max)	NA	200A (max)	450A (max)
Charge Temperature	0 to 48°C	NA	NA	-15°C to 50°C	5 to 25°C	15°C to 30°C
Connector	Wet-mateable connector	Burton connector	Seacon WET-CON	IL4FS	NA	IP67
Compensation	Inert oil	NA	NA	Inert oil	NA	NA
Enclosure material	Stainless steel	Aluminum	Rugged enclosure	Polyethylene	NA	NA
Communication	NA	NA	RS485/MOBUS	NA	NA	Modbus/TCP

2. Underwater Lithium-ion Battery Power System Design

The Lithium Iron Phosphate (LiFePO4) battery consists of twelve CAM50F LiFePO4 cells (see Table 2). The cells were made by China Aviation Lithium Battery (Luoyang) Co., Ltd. The battery's dimensions are as follows: 135mm long×29mm wide×222mm high and has a mass of 1.9kg. The BMS includes a smart battery management system (BMS) with energy management, thermal management, and protection system. The BMS has the following functions: battery state of charge (SOC) estimation, state of health (SOH) estimation, and active cell balancing. The thermal management monitor and reduce the ambient temperature within the enclosure. The protection system regulates the power input to different circuit board and isolates the power electronics from the load. It also helps to control and convert the Direct Current (DC) voltage level to different voltage levels (via a DC-DC/Alternating Current (AC) converter) to 24 V and 48 V. The communication with external devices via RS485 and MODBUS are also included. The charger will charge the unbalanced cells in the battery pack.

Table 2: Specifications of CAM50F LiFePO4 prismatic battery cell

Descriptions	**Specifications**
nominal capacity	50 Ah
nominal voltage	3.2 V
maximum constant discharging current	50 A
standard charging current	15 A
discharging cut-off voltage	2.5 V
charging temperature	0℃ to 45℃
discharging temperature	-20℃ to 50℃

The single cell has a 3.2 V and capacity of 50 Ah. In the proposed design, the battery pack consists of 12 cells connected in series to achieve a battery power density of 2 kWh in a compact pressure-resistance enclosure for 3000 m of seawater. As the designed power supply system will be exposed to the deepwater, proper sealing is required to prevent water leaking into the system. An O-ring is used in sealing pressurized systems up to a pressure equivalent to 3000 m. They are mounted at the top of the enclosure fastened by few mechanical bolts. The electrical connectors will be assembled near to the enclosure cover for subsea connectors. Figure 1a shows the schematic of the electro-mechanical systems architecture layout.

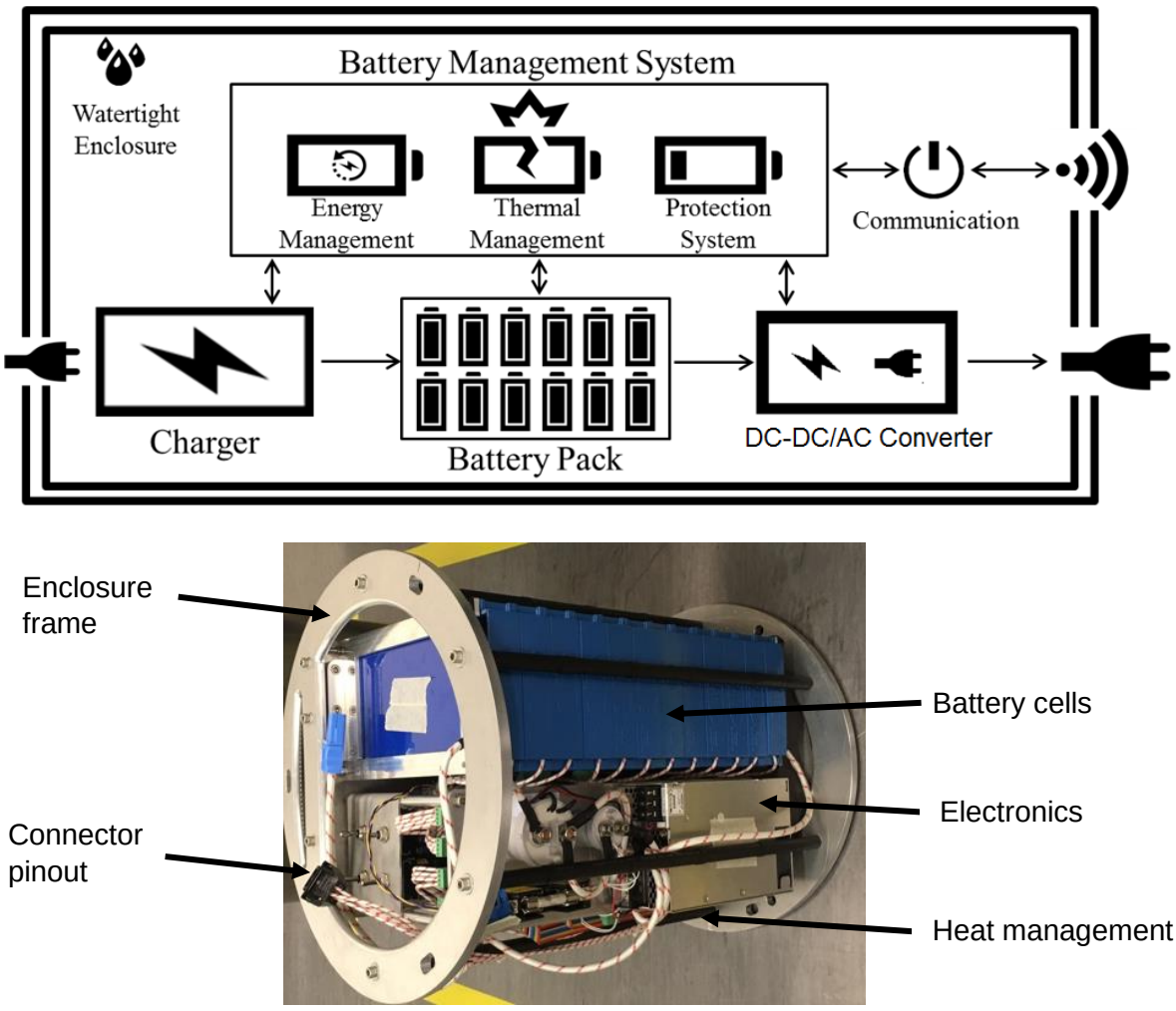

Figure 1. (a) Overall electro-mechanical systems architecture design for underwater battery power system; (b) interior layout of battery power system

2.1. Mechanical and Electronic Systems Arrangement

The inner arrangement of the LiFePO4 battery power supply system can be seen in Figure 1b. The battery power system is developed to accommodate all electronic devices and battery cells. The internal volume is separated into five main layers namely: battery, connectors, enclosure, electronics, and thermal management system. The horizontal orientation of the battery power system will facilitate installation on board of ROV.

In the proposed SOC estimation and active cell balancing, a bidirectional DC-DC/AC converter is used to interface between the battery and the load. With the power demand from the load, the main control module also computes the values of the voltage and current needed. The terminal voltage of the

battery will be tuned for maximum efficiency of the converter. The online SOC estimator based on Ah counting uses the data obtained from the sensor. As seen in Figure 2a, the sampled data are transferred to the microprocessor (via serial port) for SOC estimation and cell balancing (via active balancing and protection circuit) in Figure 2a. The front-end connection circuit provides the interface between the external circuits to the main control board. The programs are coded in C++ via MPLAB software that interface to the computer.

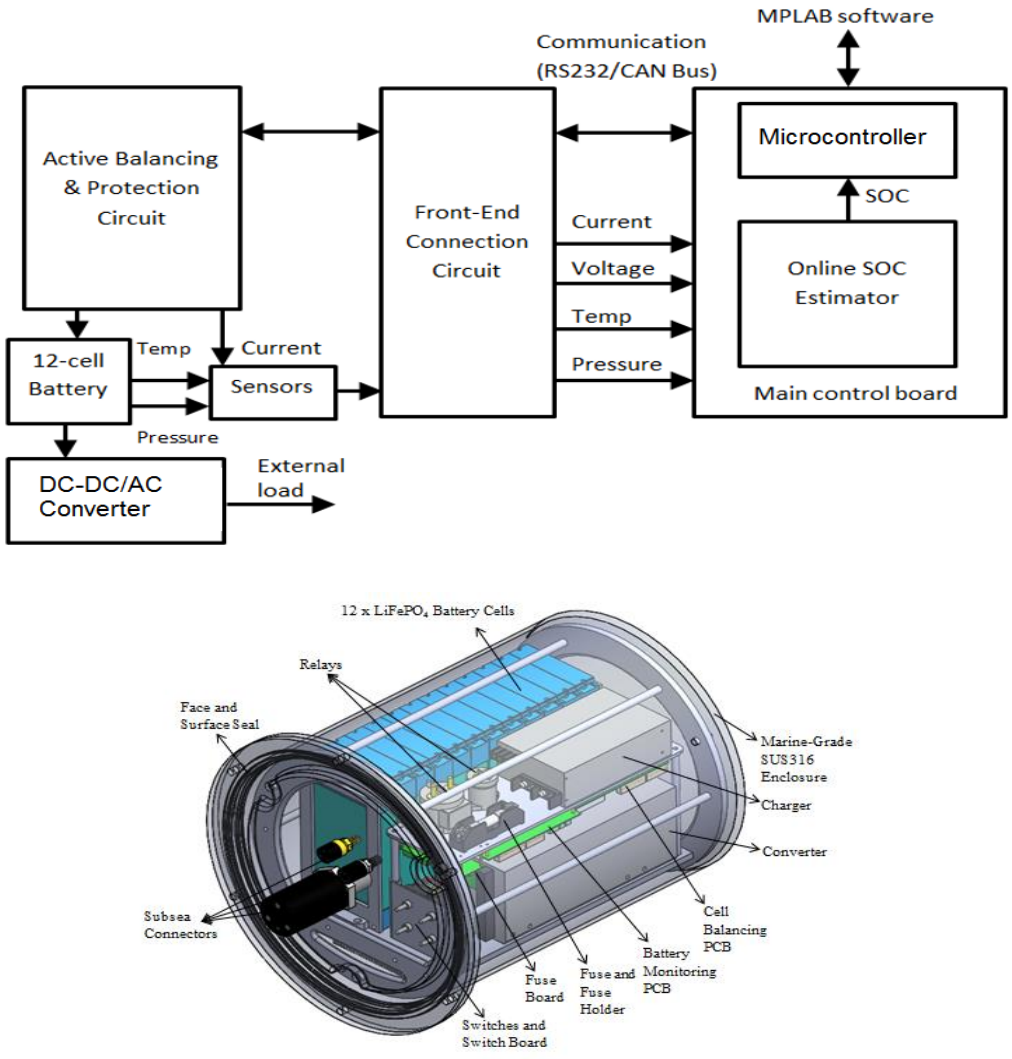

Figure 2. (a) Schematic layout of active cell balancing, SOC estimation and interface for underwater battery power system; (b) Overall view of battery power system [7]

The overall view of the computer-aided design (CAD) model can be seen in Figure 2b. The enclosure is in a cylindrical geometry adapted for the high-pressure vessel design. The supporting structure within the enclosure also strengthens the flat end plates to prevent premature buckling due to high hydrostatic pressure. It also help to eliminate the need of hemispheric end plates that are difficult to fabricate. The majority of the thermal heat will be produced by the LiFePO4 battery cells and power electronics during the charge and discharge process. Due to the weight of the battery cells, its natural orientation would be at the bottom. During operation, the heat generated from the power electronics and battery cells would heat the surrounding air within the enclosure. The heated air accumulates at the top of the sealed chamber due to convection. Hence, the power electronics are fitted with fans to create a force circulation for driving the hot air towards the cooling heat sink to cool the interior space. It is thus more energy efficient than an active thermal management system that requires liquid-based cooling system.

The final mechanical specifications of the battery power system (see Figure 2b) are 0.63 m long and 0.44 m width. The mass in the air is approximately 90 kg and 23 kg in water. The three-dimensional (3D) model depicts the arrangement of all the components within the watertight enclosure and cover. The components are arranged to consume less space. All the parts are assembled in such a manner to reduce wiring and hence lowered the resistance and increased efficiency. Safety and reliability of the battery power system such as automatic cut off are in-corporated. In addition, fire retardant wires are used to prevent fusing and shorting of the batteries during high current drawing and surges. The details of the layers can be seen in Figure 2b.

2.2. Battery Layer

The battery module consists of the twelve CAM50F LiFePO4 cells arranged in series as seen in Figure 2b. The stack is secured via two top and bottom plates that are bolted down onto the frame inside the battery enclosure. It ensures the stability of the system and minimal movement during transportation and application. The arrangement also allows greater space savings and ease of connection between battery cells. The battery holders allow a small gap within each battery cell to

compensate for the inevitable expansion of the battery cell and help to dissipate the thermal heat generated by the batteries during the charging and discharging.

2.3. Power Electronic Layer

The assembly including the power electronic layer is shown in Figure 2b. The power electronics consists of a few major components: charger, converter, relays and control boards. The converter is used to convert the DC voltage of the battery to some DC and AC output voltage. The charger is built to recharge the battery cells after the discharging. A few relays are integrated into the system to cut off the power during extremely high battery cell temperature, high current or extremely low voltage in the battery system. They are used as a safety device to prevent further damages to the system. There exists three printed circuit boards attached to the horizontal support plate. There are namely: battery monitoring board, cell balancing board, and the fuse board. The structure inside the enclosure provides sufficient support for the electronics.

2.4. Connectors Layer

To connect the battery power system to the underwater vehicle, subsea connectors are used. Three connectors are used, namely, charger connector, communications connector, and output power connector. These rubber molded subsea connectors are rated for 13700 m and can withstand up to 600 VDC and 300 A. They are made of neoprene; glass enforced epoxy, stainless steel, and Delrin.

2.5. Enclosure Layer

The battery supply system will be operating in subsea conditions with harsh pressure and temperature. It is vital that the system is fitted with features to prevent water leakage. The O-ring is fitted within a groove of the top cover and sufficiently compressed when the cover is tightened. The thickness of the O-ring is 6 mm and has a compression rate of 25 %. The O-ring can withstand pressures up to 300 bars (~3000m). The enclosure and cover are made of SUS 316 marine grade stainless steel.

As compared to common subsea enclosures such as aluminum and titanium, SUS316 stainless steel has relatively good strength to weight ratio with reasonable cost.

There are many considerations in the design of the subsea enclosure that houses the battery power system. The factors include shape, depth rating, and overall weight. The cylindrical shape provides equal distribution of stresses with less sharp corners. The thin-walled pressure vessel is considered to be thin-walled if its wall thickness, t_w, to vessel radius, R, is less than 1 ($t/R << 1$). The battery power system enclosure consists of a thin-walled cylindrical body with flat end caps. The cylindrical coordinate system (x, r, θ) is used, where x represents the axial coordinates, r represents the radial coordinate and θ represents the angular coordinate. The cylindrical body experiences stress in the circumference and axial directions due to the axisymmetric characteristics. The stress in the circumference is called hoop stress, σ_θ, and the stress along the axial direction is called longitudinal stress, σ_x. The hoop stress is the force exerted on the circumference of the cylinder. It is twice as high as the axial stress. Therefore, the hoop stress is the main factor in the design. The formulas for the stress components σ_θ and σ_x are written as follows.

$$\sigma_\theta = \frac{P\,R}{t_w} \tag{1}$$

$$\sigma_x = \frac{P\,R}{2t_w} \tag{2}$$

where P is the pressure acting on the cylinder, R is the radius of the cylinder (for thin-walled pressure vessels, $R=R_I = R_O$) and t_w is the thickness of the cylinder wall.

The calculated maximum pressure (without safety factor) of the 316 stainless steel cylindrical thin-walled pressure vessel is 145 MPa that correlates to 1450 m water depth pressure. However, the weakest point of the design is not the cylindrical body. It is the top cover of the enclosure. The current depth rating depends on the maximum pressure applied on the top cover. The thickness of the flat end cap can be computed as follows.

$$t_f = d\sqrt{0.3P/S} \tag{3}$$

where t_f is the thickness of the flat end head or cap (mm), d is the inner diameter (mm), P is the applied pressure (MPa), and S is the maximum allowable stress (N/mm^2).

By using (3), the thickness of the flat end cap can be computed as 10 mm for a maximum pressure at the flat end cap of around 12 MPa (or 120 m water depth pressure). To fulfill the 3000 m depth of seawater, the cylindrical body and end cap thickness should be around 10.5 mm and 50 mm thick, respectively.

2.6. Thermal Management System

The two main factors to consider in thermal management system are the surrounding temperature and humidity within the enclosure. The proposed thermal management system comprises of two main parts. The thermal storage unit and the humidity storage unit. The thermal storage unit consists of fins, cover plate, honeycomb, phase change material, gasket, and base plate. The humidity storage unit includes the desiccant cover, desiccant and base plate. The thermal storage unit combined a finned heat sink and a phase change material (PCM) for thermal storage. The aluminum honeycomb structure within the hollowed base plate to improve the heat transfer between the fins and the PCM. The high latent heat storage capacity of the PCM makes it favorable to store large amounts of heat emitted from the battery cells and power electronics. With sufficient heat energy, PCM changes phases and melts into a liquid. When the heat source is removed, it dissipates the heat and solidifies back to its original state. The melting point of the phase change material is 35 °C. The batteries will be kept constant at 35 °C. If the system requires to be held at a lower or higher temperature, a suitable melting point of PCM could be used to replace the existing one. The humidity storage unit holds a packet of the desiccant within a perforated cover and the base plate to prevent condensation on the sensitive power electronics. The system takes advantage of the existing cooling fans on the power electronics to create an environment of forced ventilation in the enclosure that channels the hot and moist air to the thermal and humidity control system.

3. Thermal System Design

A thermal simulation based on conjugate heat transfer module was performed on the battery power system via COMSOL Multiphysics 5.3. It was used to solve the battery system model presented in this paper. The model consists of conjugate heat transfer physics, multiple heat sources and atmospheric temperature. The outputs of the model are the surface temperatures of each component and ambient temperature. The PARDISO time-dependent solver with a relative tolerance of 0.01 was chosen for all the variables; solutions were tested for mesh independence and the solution time for this model was approximately 35 minutes by a computing platform with 4-core processors (2.60GHz) and a total of 4 x 8 GB RAM (random access memory). The mesh of the model is composed of 133,160 elements with a minimum element quality of 0.00172. The primary boundary conditions of the analysis are as follows:

- Laminar Flow -Internal and external fluid flow
- Heat Transfer –Solid, Liquid, Heat Source (electronic components) and Boundary Temperature (external ambient temperature)
- Time-dependent
- Simulation time of 3600 s with 60 s step size
- Initial temperature of 298 K or 277 K (25 °C or 4 °C)
- Initial pressure of 1 bar
- Battery discharge rate of 1 C (50 A)

The simulation was based on the operational conditions of the battery power system at subsea depths (at 4 °C outside the enclosure) as well as normal land conditions (at 25 °C outside the enclosure). Both conditions used the discharged at constant 50 A(1 C) for 1 hour (full discharge).

The battery cells give off heat during their charging or discharging cycles via electrical heating (Joule heating effect) and thermochemical heating effect. Due to the complex thermochemistry of the Lithium cells and the unstable thermic reaction, its effect was ignored. The more significant heating effect, the Joule heating effect, often referred to as resistive loss, occurs when there is a current flow

through a resistive element. In the battery, heat is dissipated through the resistive properties of the battery cell, i.e. battery internal resistance. The Joule heating effect, Q_{Joule} is described as:

$$Q_{Joule} = I^2 R_i \tag{4}$$

where I is the current (A) and R_i is the internal resistance of the battery (Ω).

The standard time-dependent heat transfer equation [36-37] is as follows:

$$\rho C_P \frac{\partial T}{\partial t} + \rho C_P u \cdot \nabla T = \nabla \cdot (k \nabla T) + Q \tag{5}$$

where $\boldsymbol{\rho}$ is the density (kg/m^3), $\boldsymbol{C_P}$ is the heat capacity at constant pressure (J/kgK), T is the temperature (K), $\boldsymbol{u}$ is the velocity field (m/s), $\boldsymbol{k}$ is the thermal conductivity (W/mK) and $\boldsymbol{Q}$ is the heat source (W/m^3).

The software, COMSOL uses the Navier-Stokes equations to govern the motion of fluids. In the case of a compressible Newtonian fluid, the equation is as shown.

$$\rho \left(\frac{\partial u}{\partial t} + u \cdot \nabla u \right) = -\nabla p + \nabla \cdot \left(\mu (\nabla u + (\nabla u)^T) - \frac{2}{3} \mu (\nabla \cdot u) I \right) + F \tag{6}$$

where u is the fluid velocity field (m/s), p is the fluid pressure (Pa), ρ is the fluid density (kg/m^3), μ is the fluid dynamic viscosity (Pa.s) and F is the volume force field (N/m^3). Each term of the equation represents and corresponds to the inertia forces, pressure forces, viscous forces and the external forces applied to the fluid. The Navier-Stokes equations represent the conservation of momentum while the continuity equation represents the conservation of mass. These equations are always solved together. The continuity equation is as follows:

$$\frac{\partial \rho}{\partial t} + \nabla \cdot (\rho \boldsymbol{u}) = 0 \tag{7}$$

where $\boldsymbol{u}$ is the fluid velocity field (m/s) and ρ is the fluid density (kg/m^3).

Although the experiment was not performed for this set up due to the size of the battery power system could not fit into the current thermal chamber, a similar experiment using the same CAM50F LiFePO4 cells [22] was performed in a different enclosure (made of acrylic material). The purpose is to verify the accuracy of the thermal simulation performed in the COMSOL on the same cells used in the proposed battery power system. The setup is shown in Figure 3a. The results obtained in the thermal

simulation were compared with the experiment results in order to validate the accuracy of the simulation results at different locations as shown in Figure 3b. The maximum temperature of the simulation and experimental results are tabulated in Table 3. It shown a maximum error between the simulation and experimental results is approximately 1°C. The maximum simulated temperature is at the top of the battery stacks (i.e. at Point 4). As compared to the thermal responses obtained from the experiments (see Figure 4), the maximum temperature [22] is also located at Point 4. The simulated temperature is approximately 29.3°C (i.e. 0.5°C above the experimental value of 28.8°C). Note that both the simulated and experimental values are below the discharging current limit of 50°C in Table 2. However, it has been observed that there is a drop in temperature during the period from 4000 s to 8000 s. It can be caused by a negative entropic heat contribution in a lithium type battery [38]. In summary, the simulated results closely matched the experiment results with a root mean squared error of around 2.45%.

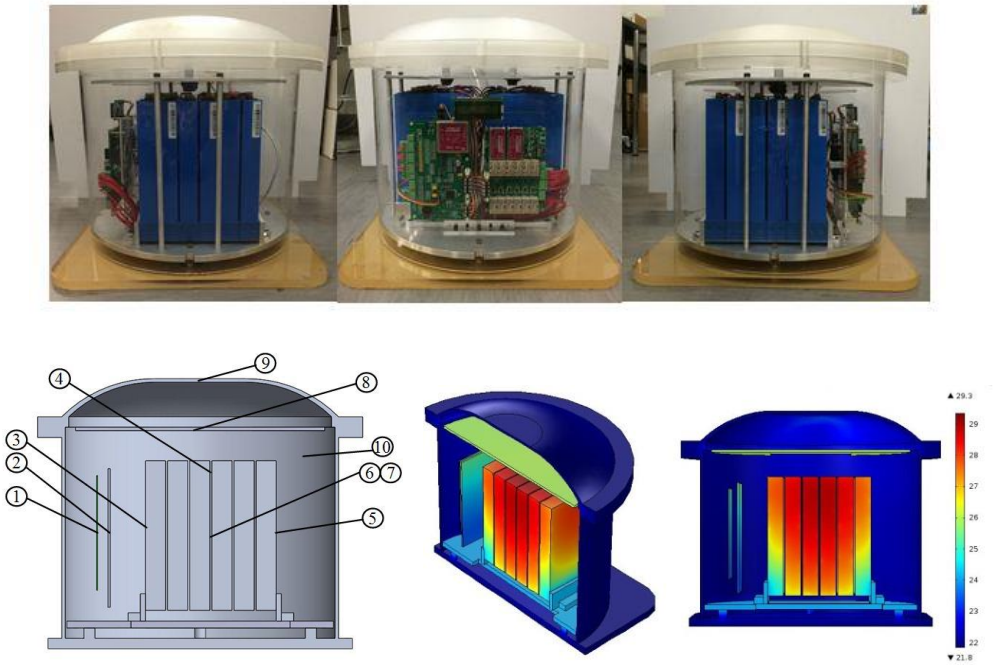

Figure 3. (a) Experimental setup for thermal validation of CAM50F LiFePO4 cells [22] (b) measurement locations and COMSOL results [22]

Locations	**Simulation (°C)**	**Experiment (°C)**	**Error (°C)**	**Error** $\left(\frac{\text{simulation-experiment}}{\text{experimental}}\right)\times 100$ **(%)**
1	24.2	23.5	0.7	3.0
2	24.2	23.9	0.3	1.3
3	27.1	26.4	0.7	2.7
4	29.3	28.8	0.5	1.7
5	27.1	26.4	0.7	2.7
6	28.0	27.9	0.1	0.4
7	28.3	27.6	0.7	2.5
8	25.9	25.2	0.7	2.8
9	22.5	22.7	0.2	-0.9
10	25.1	24.1	1.0	4.1

Table 3. Simulation vs. experimental results (maximum temp) [22]

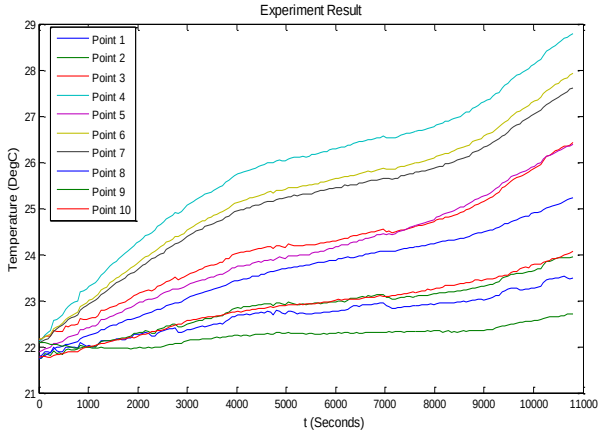

Figure 4: Results of thermal responses at various locations during experiment [22]

By applying the similar approach to the proposed battery power system, the thermal simulation as shown in Figure 5a and Figure 5b can be obtained. The main heat sources are the battery cells, converter and the components on the printed circuit board (PCB). The low subsea temperature sufficiently cools the enclosure, and through natural convection within the enclosure, reduces the temperature of the core electrical components. In the worst case scenario in Figure 5b, the battery cells reach a maximum temperature of 54 °C that is still under the safe operating temperature range provided by the manufacturer. As shown in the simulation results (see Figure 5c), the battery cells positioned in the row operates at an average temperature of 30 °C (within the temperature stated by manufacturer).

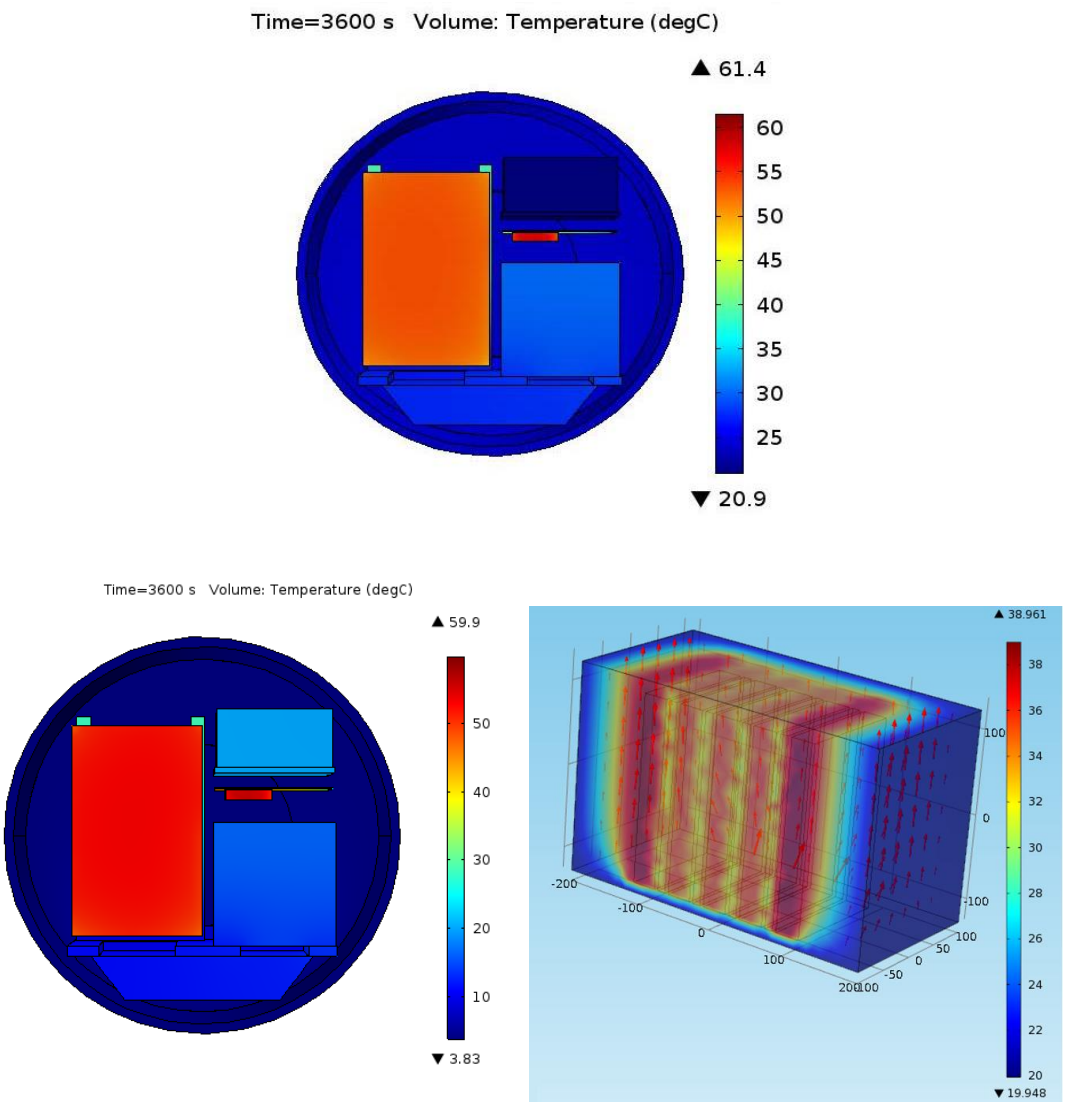

Figure 5: Thermal simulation of underwater battery power system using CAM50F LiFePO4 cells (a) on land condition at 25 °C); (b) subsea condition of 4 °C; (c) battery cells in series position

4. Smart battery management system (BMS) design

The smart battery management system (BMS) includes the algorithms for active cell balancing, SOC and SOH estimation as well as real-time system monitoring of the battery stack. The BMS also measures and stores all the cell voltages, the battery temperature and the current. During operation of the BMS, data on current, cell voltages and battery temperatures of the power source will be transmitted to surface computer for analysis.

4.1. Battery Parameters Estimation

An accurate SOC estimation could improve the performance and reliability, and lengthen the lifetime of the battery. The SOH indicates the "health" of the battery such as the life cycle of the battery and its condition relative to a fresh battery from factory. The conventional method to estimate both the SOC and SOH is Ah counting or coulomb counting method. Although this method is susceptible to current measurement errors due to its integration over time, it is simple to use and apply in actual application. Alternate methods such as voltage-based method and impedance-based method have been used. An adaptive based technique using Kalman-based filter [15] was often used to cater for uncertainties. However, Kalman filter is a recursive method that requires iteration that could increase the computation time that leads to longer balancing time of each battery cell after the SOC values are estimated.

Figure 6 shows a second-order battery model. C_1 and C_2 are very huge capacitors in kF. In the proposed method, it is assumed that the voltage drops across C_1 and C_2, during short duthe ration of charge or discharge, does not change much and they are neglected. R_0, R_1 and R_2 are obtained from the discharge and relax cycle of the battery. The battery under test is fully charged and is subjected to a 0.3 C (15 A) discharge cycle.

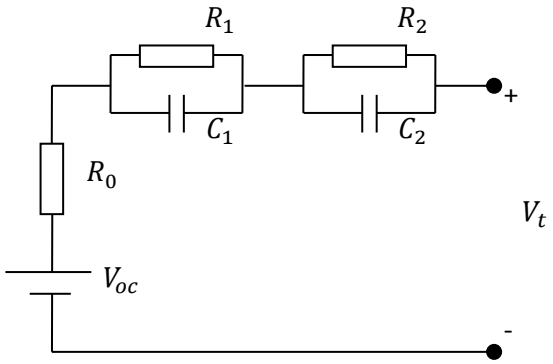

Figure 6: Second Order Battery Model

The 2RC parameters at different SOC were determined from the pulse discharge test. The test generated a series of discharge current pulses of 15A for decreasing SOC values. During the test, the battery was first charged to 15 A to the fully charged state in constant current-constant voltage (CCCV) mode to around 3.5 V. Then discharging the battery cell at a pulse current 15A for 15 s, relax for 300

s, discharge for 1200 s and then relax for 1 hour until the terminal voltage reaches the cut-off voltage of 2.5 V. The open circuit voltage (OCV) was then obtained when the battery's terminal voltage reached equilibrium state during the relaxation period. The values of the SOC and SOH were estimated via the standard Ah counting method. The values of 2RC parameters are then obtained as follows.

The terminal voltage response was plotted using MATLAB curve fitting tool that fitted equation (8).

$$y = a - be^{-ct} - de^{-ft} \tag{8}$$

where coefficients a, b, c, d and f are known after the curve fitting. The coefficients a, b, c, d and f correspond to (9) to (14) respectively.

$$V_t = V_{OC} - V_1(0)e^{-t/R_1C_1} - V_2(0)e^{-t/R_2C_2} \tag{9}$$

$$V_{OC} = a \tag{10}$$

$$V_1(0) = b \tag{11}$$

$$V_2(0) = d \tag{12}$$

$$\frac{1}{R_1C_1} = c \tag{13}$$

$$\frac{1}{R_2C_2} = f \tag{14}$$

Substituting (11) and (13) into (15), R_1 is computed with pulse discharge duration, $t = t_d = 15s$ and discharging current, $I = 15$ A.

$$IR_1(1 - e^{-t_d c}) = V_1(0) \tag{15}$$

Similarly, R_2 can be computed by substituting (12) and (14) into (16).

$$IR_2\left(1 - e^{-t_d f}\right) = V_2(0) \tag{16}$$

The resistance, R_0 can be obtained by taking the average resistance at the beginning and the end of the 15 s pulse discharge cycle. This can be performed by taking the voltage difference at end of the 1 hour relax cycle and beginning of the 15 s pulse discharge cycle divided by the discharge current. With R_1 and R_2 obtained, the capacitance, C_1 and C_2 can be computed via (13) and (14), respectively.

The total internal resistance, R_i, is the sum of R_0, R_1 and R_2. Since the internal resistance of the battery varies at different SOC, ten sets of total internal resistance are extracted at SOC from 10 % to 100 % at an interval of 10% SOC. The total internal resistance, R_i depends on the SOC of the battery. The estimate of SOC will be computed via the Ah counting method. The relationship between the SOC and OCV can be obtained by finding the best curve that fitted the experimental data as shown in Figure 7 and equation (17). In addition, the instantaneous power (= OCV × current) of the battery can be determined. The OCV at different SOC values will be stored as a two-dimensional lookup table in the microcontroller.

$$V_{oc} = 3.1568 - 0.011/SOC - 0.0035SOC + 0.0025\ln(SOC) - 0.0397\ln(1-SOC) \quad (17)$$

where ln is the natural logarithm.

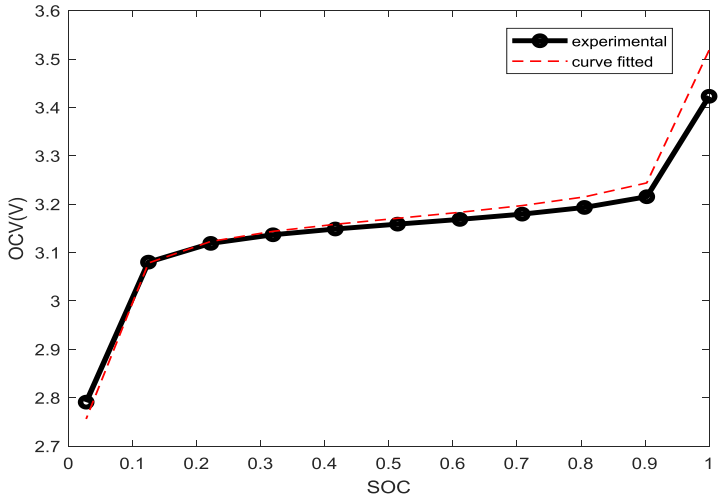

Figure 7: OCV-SOC relationship curve

In this paper, the state-of-health (SOH) of a battery is estimated using the Ah counting method.

$$SOH = C_{\max}/C_{rated} \times 100\ \% \quad (19)$$

where C_{rated} is defined as the measurement of the charge and discharge current with respect to its nominal capacity (the value is typically given by the manufacturer) and C_{max} is the maximal releasable capacity.

4.2. Active Cell Balancing Design

The balancing routine is used to check for cells that are not balanced and to perform the active cell balancing. The flowchart of the balancing routine is shown in Figure 8a. Firstly, the balancing routine will find the lowest, highest and average SOC of each cell. The cell with the lowest and highest SOC will be recorded. Secondly, the balancing routine will determine whether the BMS has been balanced by using the lowest, highest and average SOC. If all the cells are balanced, the balancing routine will turn off the relays that control the active cell balancing. Thirdly, the balancing routine will activate the active cell balancing for the cell with the lowest SOC. Two DC-DC converters are used in the active cell balancing. One DC-DC converter will be used to balance Cell #1 to #6 and another DC-DC converter will be used to balance Cell #7 to 12. The DC-DC converter used to balance Cell #1 to #6 is powered by Cell #8 to #12 whereas the DC-DC converter used to balance Cell #7 to 12 is powered by Cell #1 to 5. The balancing routine will turn on the relays that connect the necessary cells to activate the desired DC-DC converter. In addition, relays will connect the cell with the lowest SOC to the DC-DC converter.

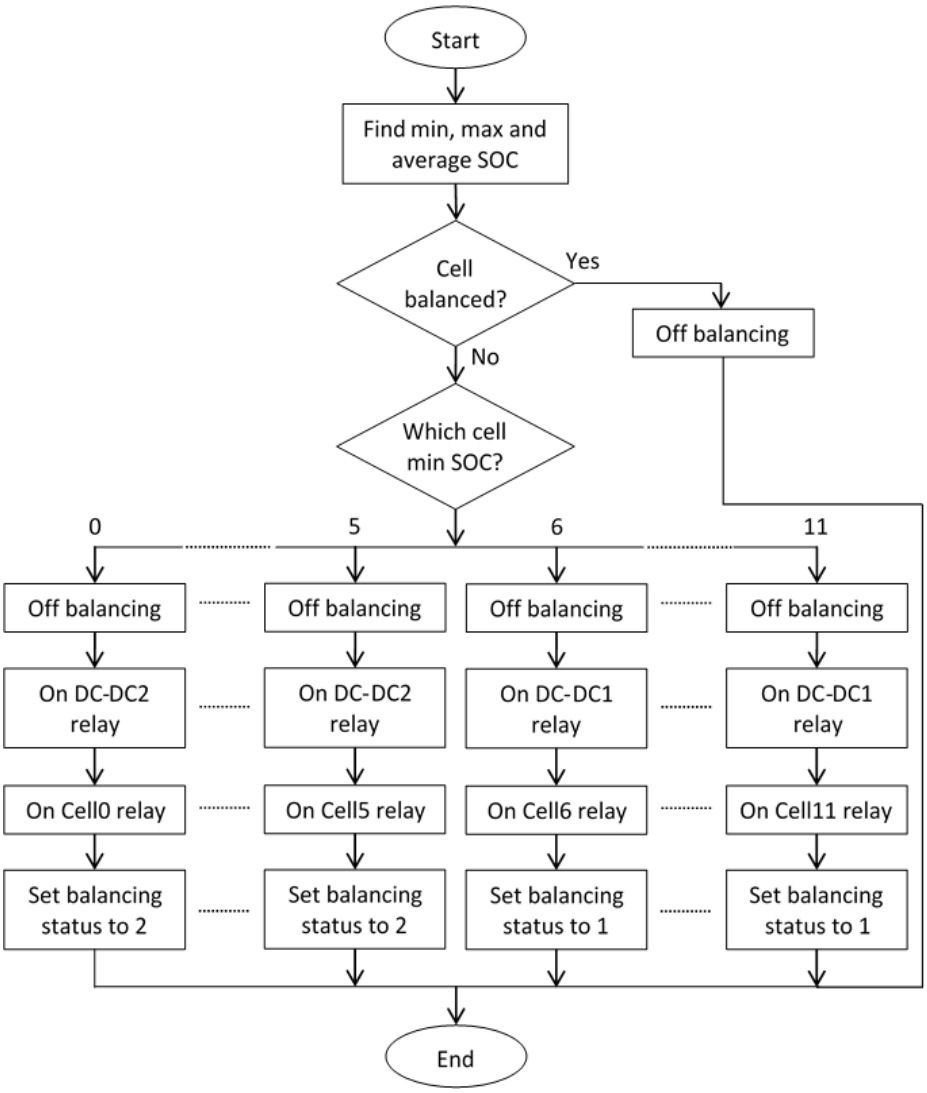
Start
Find min, max and average SOC
Cell balanced?
Yes
Off balancing
No
Which cell min SOC?
0
5
6
11
Off balancing
Off balancing
Off balancing
Off balancing
On DC-DC2 relay
On DC-DC2 relay
On DC-DC1 relay
On DC-DC1 relay
On Cell0 relay
On Cell5 relay
On Cell6 relay
On Cell11 relay
Set balancing status to 2
Set balancing status to 2
Set balancing status to 1
Set balancing status to 1
End

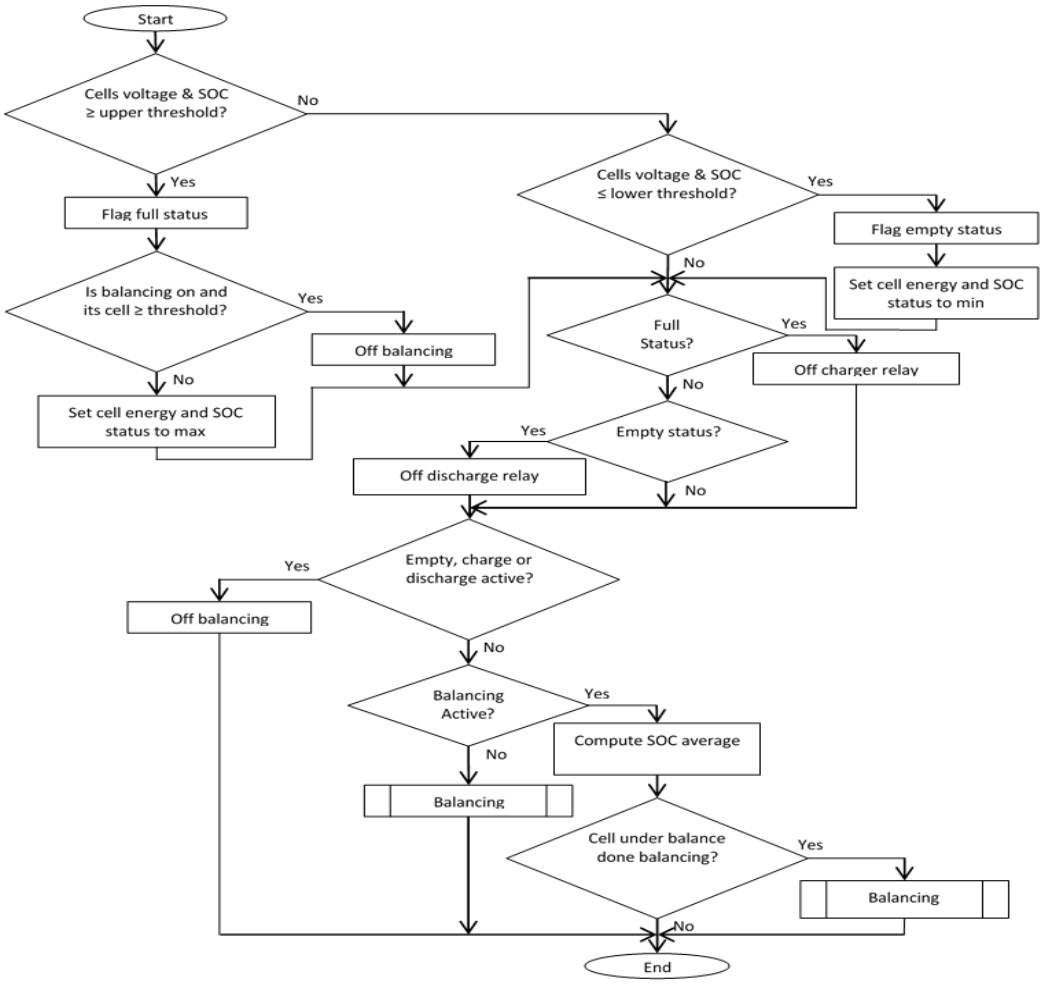

Figure 8: Flowchart for (a) cell balancing; (b) cutoff control flowchart

The cutoff control routine controls all the relays on the balancing PCB. As shown in Figure 8b, the routine uses the acquired batteries voltage and the computed SOC to determine whether to switch off the relay. When the voltage and computed SOC reach the upper threshold, the relay that connects the battery pack to the charger will be turned off to terminate the charging. In addition, if the BMS is performing the active cells balancing, the active cells balancing process will be turn off. It helps to prevent the batteries from overcharging. When the voltage and SOC drop to the lower threshold, the relay that connects the battery pack to the DC-DC converter will be turned off. The routine uses the current readings from the transducer to detect charge or discharge activity. It will turn off the active cell balancing process when there is a charge or discharge activity. If there is no charge or discharge activity,

the SOC of the cells used in the balancing process will be updated. The balancing routine will execute to check for any cells that are not balanced in order to repeat the entire cell balancing process. In short, the cutoff control routine controls the relays to protect the batteries. It also updates the SOC of the cells and determines whether the batteries require balancing.

The battery data such as SOC values and balancing status of each cell are sent to LabVIEW VI graphical user interface (GUI). The frame structure of the data packet to LabVIEW VI GUI from the microcontroller (MCU) is shown in Table 4. A 4 bytes Gold code will be sent to the LabVIEW VI GUI followed by the individual cell voltages and the packet error check (PEC). The different cell voltages are 18 bytes, and the PEC is 1 byte for LTC6803-4 battery stack monitoring chip. The individual cell voltages are 24 bytes and the PEC is 2 bytes if LTC6804-2 battery stack monitoring chip is used. The temperature, pressure, battery stack current and PEC will be the next data to be sent. Followed by SOC, balancing status, cell ID under balancing, balancing DC-DC converter input current, balancing DC-DC converter output current and the PEC.

Table 4: Data frame structure of MCU to computer

4 Bytes	18-24 Bytes	1-2 Bytes	6 Bytes	1-2 Bytes	30 Bytes	1-2 Bytes
Gold Code	Cells Voltages	PEC1	Temperature (2), Pressure (2), Stack Current (2)	PEC2	SOC (24), Balancing Status (1), Cell ID Under Balancing (1), Balancing DC-DC Converter Input Current (2), Balancing DC-DC Converter Output Current (2)	PEC3

4.3. User-Interface Software Implementation

The LabVIEW VI GUI was developed to display the status of the BMS. It will show the voltage and SOC of all 12-cell. Besides, battery pack total voltage, current, temperature pressure, and cell balancing status are included in the GUI. It can issue command to charge the cells and activate the cell balancing. The LabVIEW VI GUI checks for charge enable command. If the charge is allowed, the GUI will send a charge command to the MCU for necessary actions. The GUI will check the serial com port and receive any incoming data byte. With no incoming data, the GUI loops back to check for charge

enable command. If the data byte is received, it will be stored in an array. The GUI will check the array for the Gold code header. If Gold code header is not found, the GUI will loop back to check for charge enable command. Otherwise, the GUI will continue to receive the entire packet of data. PEC will compare with the received PEC. If they do not match, the array containing the received data will be cleared and the GUI will then check for charge enable command. If there is no error in the PEC, the GUI will process the received data and update the display. The Gold code and the PEC checking will ensure that the received data have no error in the received packet for GUI. The GUI then checks whether data logging is enabled for the processed data to be written into the log file. The GUI repeats the entire process to check for charge enable command.

The GUI is a tabbed document interface with two main tabs. One of the tabs is for the graph to plot individual cells voltage over CPU time. The other tab is used to plot the graph of individual cells SOC at a different time. Serial com port selection is used for data communication. The charge function can be started by clicking the "Charge" button. By default, active cell balancing will be activated when the charging is enabled. In an event when the battery stack requires charging, the active cell balancing can be disabled by deselecting the option "Balancing when charging". It will minimize the time needed to complete the charging since the cell balancing is not utilized in this option. The information of the battery stack such as the cell voltages, SOC, battery stack current, temperature, pressure, balancing status and balancing current are logged into a tab-delimited text file.

5. Experimental Test Setup

A prototype of the battery power system was built and assembled for testing in Figure 9a. The data and power from the battery cells are transmitted via the subsea connectors attached on the cover of the enclosure. The main core modules of the smart battery management system (BMS) are the BMS monitoring printed circuit board (PCB) and the active balancing PCB. Before integrating all the hardware modules, multiple lab tests have been performed to verify the functionality of the PCBs including the algorithms embedded into BMS and the LabVIEW graphic user interface (GUI).

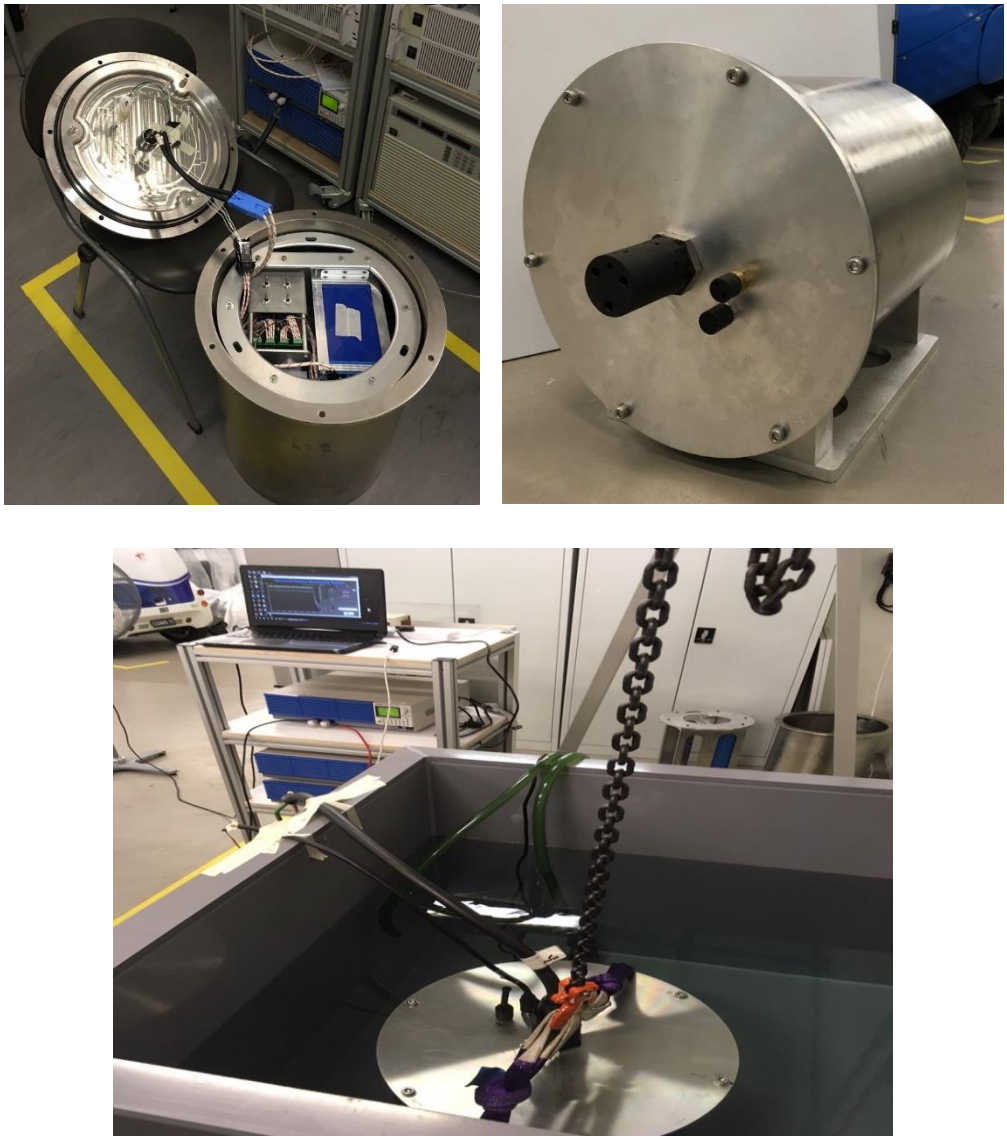

Figure 9: (a) underwater battery power system prototype views; (b) experiment setup of underwater battery power system lowered into water tank by crane

An experimental test station was set up to simulate the working conditions and environment of the battery power system. The setup aims to test the water tightness of the enclosure as well as to analyze the system performance in the cold subsea temperatures. As shown in Figure 9b, the experiment setup consists of several components such as the overhead mobile gantry crane, water tank, chilling water system, and the programmable electronic load. These components are vital to the simulation of the battery power system in its operating conditions. The water tank of size 1m × 1m × 1m is supported by a lifting crane. The tank is wrapped with thermal insulation to prevent condensation. The chilling system is capable of cooling the water down to a temperature of 4 °C from 30 °C in 14 hour and

maintaining the temperature. Thus, it simulates the temperature of seawater below 1000m. The chilling system uses R404a coolant and a titanium coil heat exchanger. The battery power system is connected via the subsea connectors up to the programmable electronic load where the battery system would be discharged in accordance to a simulated load cycle of the underwater vehicle for realistic operational conditions.

The experiment test plan for the battery power system can be tabulated in Table 5. It covers the fully-submerged and discharge of power from the battery power system. There are few risks while conducting the experiments. The water tightness of the enclosure to ensure the proper working of the safety power cut-off in the event of ingress of water into the enclosure is monitored. The battery power system was connected to the programmable electronic load via the subsea connectors and lowered into the water tank. The water tank was filled with water with the chiller in operation. Sufficient time was given to cool the water to 4 °C. The battery power system was lowered into the water tank via the mobile gantry crane.

Table 5. Experiment test plan

Description	**Objective**	**Procedure**
Fully submerging the enclosure into the water tank.	To ensure the water tightness of the enclosure.	1. Before sealing the enclosure, paste water reacting litmus paper at various locations in the enclosure. 2. Place the sealed enclosure into the water tank. 3. Ensure that the enclosure is entirely submerged. 4. Check enclosure for any air bubbles, which would indicate a leak. 5. Place desiccants in the enclosure to rule out the possibility of condensation as a leak. 6. Leave the enclosure submerged for more than an hour 7. Retrieve enclosure and open the cover. 8. Check the litmus paper within the enclosure. 9. There should not be any traces of water in the enclosure. 10. Check for color change of the litmus paper.
Discharge battery system to the electronic load, based on load cycle	To ensure the battery power system is capable of powering an industrial standard underwater vehicle.	1. Ensure that the battery cells are fully charged. 2. Programme the electrical load by the load cycle. 3. Monitor the system health and status. 4. The system should react as expected and respond accordingly if any safety issues were to arise under cut-off voltage

As observed in Figure 9b, the battery power system is completely submerged in the water tank and connected to the programmable electronic load. All CAM50F $LiFePO_4$ cells were then used to test the hardware circuitries of the BMS PCB and active balancing PCB. The CAM50F $LiFePO_4$ cells were made unbalanced. However, the cells were discharged at 0.3 C (that is 15 A) until the lowest SOC is about 50 %.

The theoretical time required for the cell to discharge from 87 % SOC to 50 % SOC at 0.3 C is approximately 4440 s. The lowest SOC cell reaches 50 % SOC at around 4600 s and active cell balancing started for the cells. At 7950 s, the cells have been balanced to within 5 % error. The terminal voltages of each cell show decreasing value as the battery was discharging until the minimal SOC is around 50%. The test results for terminal voltage and SOC during discharging are shown in the plots in Figure 10a and 10b, respectively. Note that the cell #2 and #12 are not uniform due to the poor cell quality and prolonged usage. As a result, they deviated (around 0.06V to 0.14V) from the rest of the cells during discharging. However, the responses settled to the steady-state at around 9300s. In summary, the firmware with the active cell balancing can control the relays to balance the battery stack correctly. The circuitries of the BMS PCB and active balancing PCB are functioning.

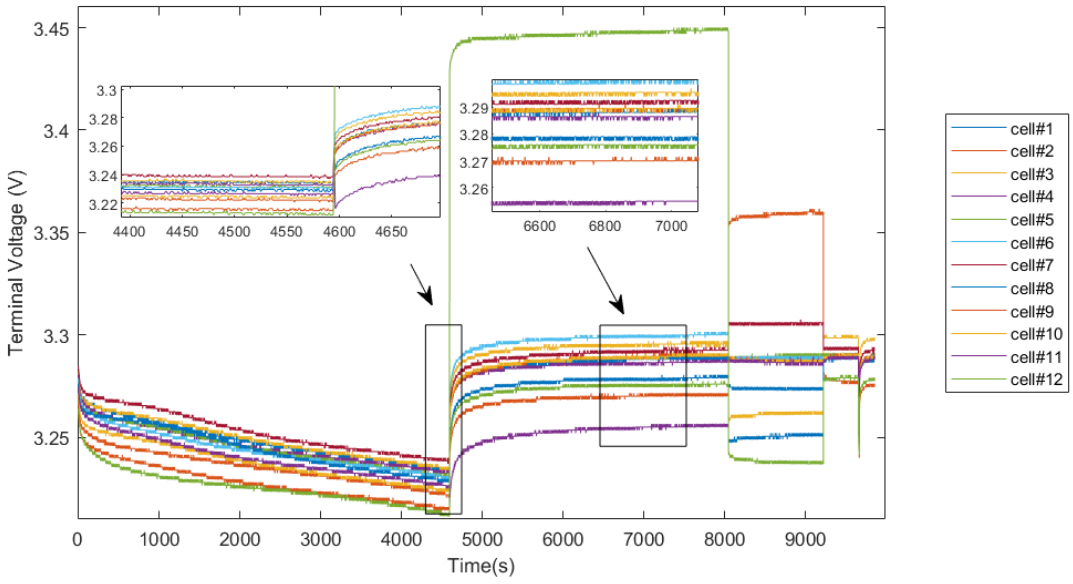

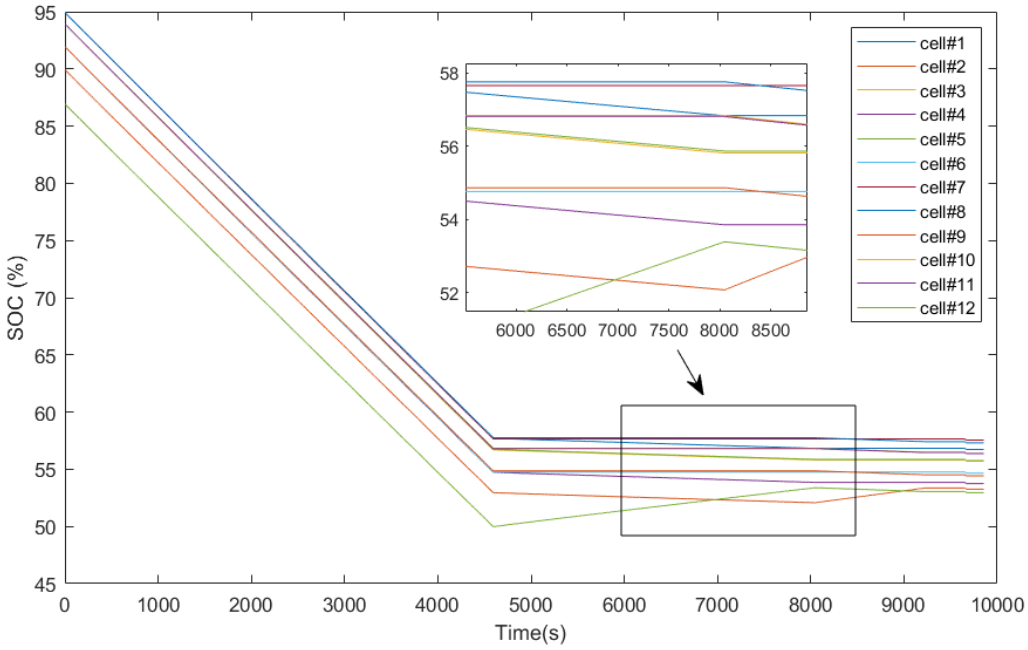

Figure 10: CAM50F (a) terminal voltage response; (b) SOC vs. time during discharge of unbalanced cells

The LiFePO4 battery pack is connected to the BMS PCB and balancing PCB through switches and fuses. The switches enable the system to isolate the PCBs from the battery pack when the system is in offline. The fuses will disconnect the batteries from the PCBs in the event of short-circuit. The battery pack is also connected to a 2 kW DC-DC converter through a 60 A fuse and a 200 A rated relay. The fuse will protect the DC-DC converter for any high current being drawn from the battery pack. The 200 A rated relay is controlled by the BMS to protect the batteries from over discharge. The battery pack is connected to a charger via another 100 A relay controlled by the BMS. The BMS system will ensure no charging and discharging activities at the same time by controlling the 100 A rated and 200 A rated relay.

5.1. Continuous Discharge Verification

All the battery cells were fully charged to 100% SOC and were discharged continuously via the 2 kW DC-DC converter. This test verified the connections from the batteries to the converter as well as

the capability of the battery pack to discharge continuously. The output of the 2 kW DC-DC converter is connected to an electronic load to draw a constant current of 20 A. The under-voltage protection is set to 2.7 V to avoid over-discharge.

Figure 11a shows the voltage of the cells against time and Figure 11b shows the SOC of the batteries (%) against time(s). The BMS stopped discharging at 9083 s as seen in Figure 11a. Since the voltage and current of the 2 kW DC-DC converter are constant, the total power delivered by the BMS is 2.42 kWh which is higher than the targeted 2 kWh. The current drawn from the batteries range from 27.15 A to 30.57 A due to the voltage of the batteries drop as SOC decreases to maintain constant power drawn by the 2 kW DC-DC converter. Due to the 2.7 V under-voltage protection, the batteries were not fully discharged. Hence, showing the cell with SOC values of 5.19% (see Figure 11b). The feature protects the batteries from over-discharge. In summary, the test successfully verified the connections between the batteries to the 2 kW DC-DC converter. The BMS is able to deliver 2 kWh and protect the batteries from over-discharging.

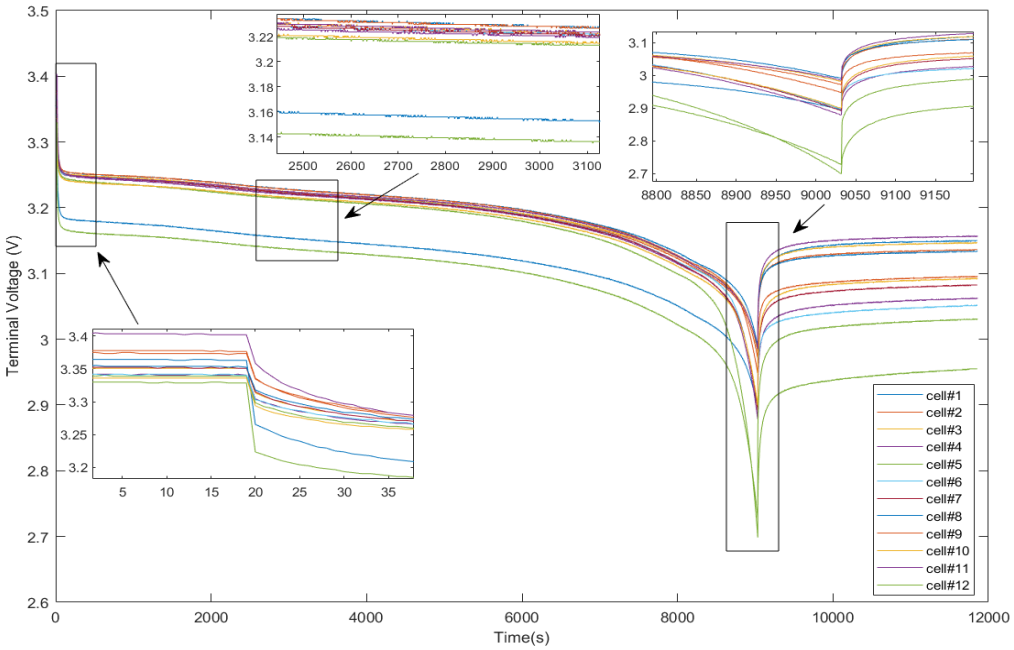

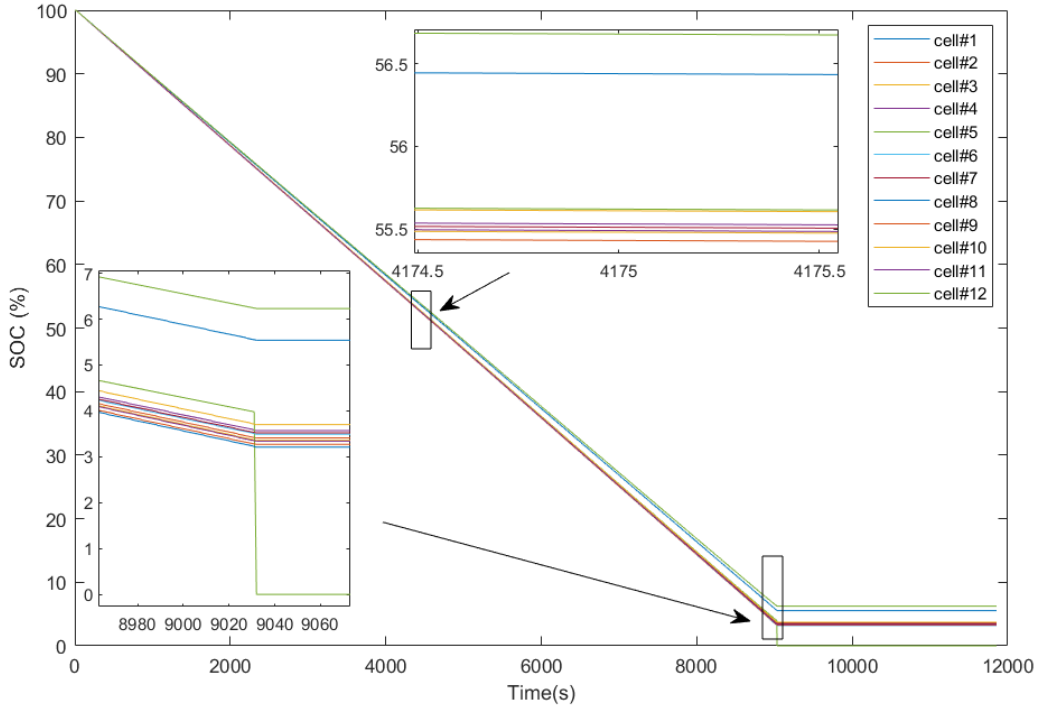

Figure 11: CAM50F (a) terminal voltage response; (b) SOC vs. time during continuous discharge verification

5.2. Charging and Active Balancing

The twelve battery cells were set to different SOC values starting from 10 % to 17.5 % as shown in Figure 12a. Figure 12a shows SOC data transmitted from the BMS. The BMS performed the active balancing at the following conditions. The cells need to have at least 30 % SOC with an average SOC difference of not more than 5 %. The SOC of each cell should not be more than 70 %. The last condition is set to enable efficient charge transfer. If the SOC is high, charge transfer will take a longer time to balance the cells. Note that the pressure in the enclosure is around 1 bar.

Due to the conditions to activate the active balancing algorithm, the minimum initial SOC of the cells was set to 10 %. The cells are charged to 30 % SOC, and active balancing is then activated. Figure 12b and Figure 12c show that the BMS is charging the cells to certain SOC levels. After the cells are balanced, the voltages of each cell are quite close to one another (see Figure 12d). The average variation of SOC for all the cells is within 5 % as shown in Figure 12e. The test successfully verified the connections between the charger to the battery pack, the capability of the charger to charge the

battery cells and the functionality of the active balancing circuitry and algorithm for balancing the battery cells.

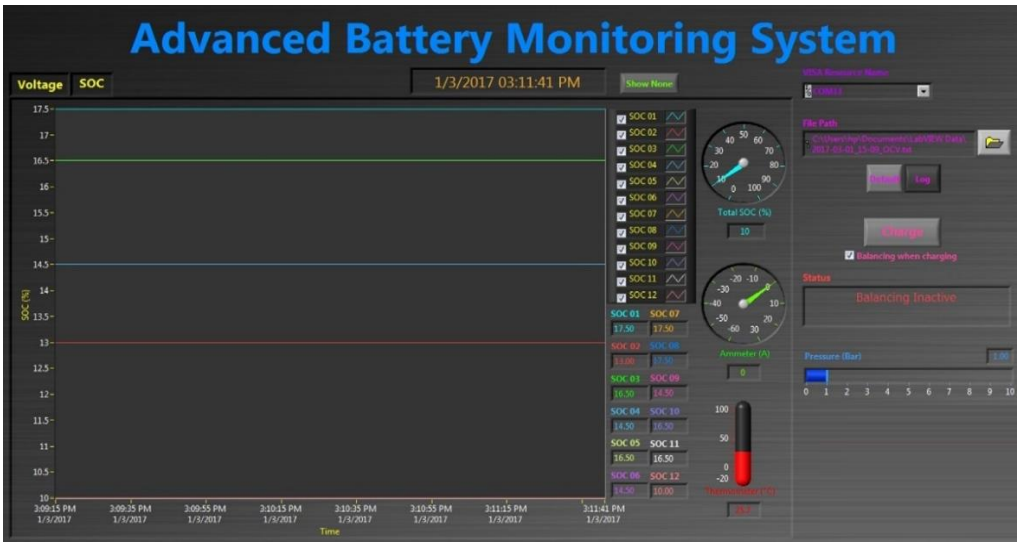

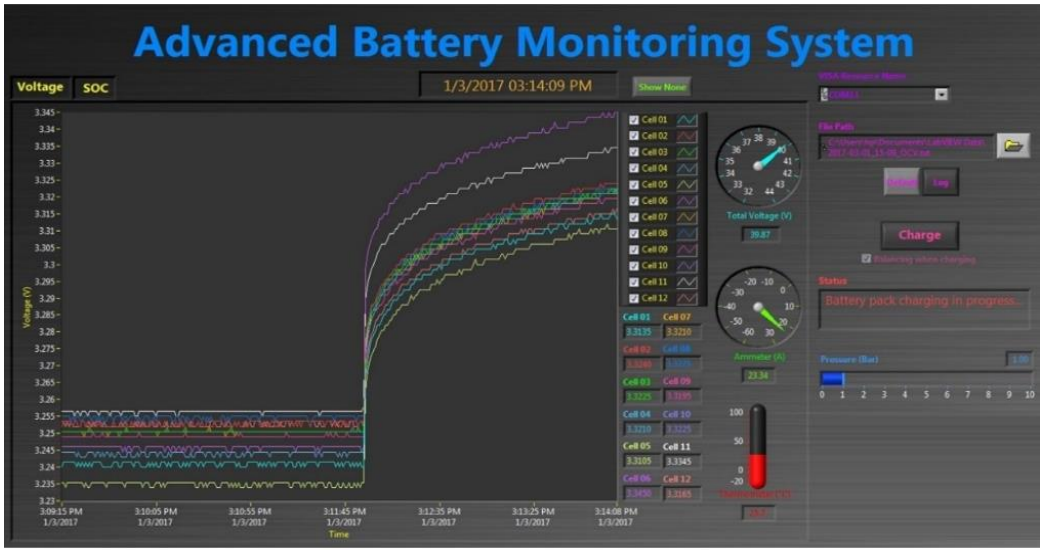

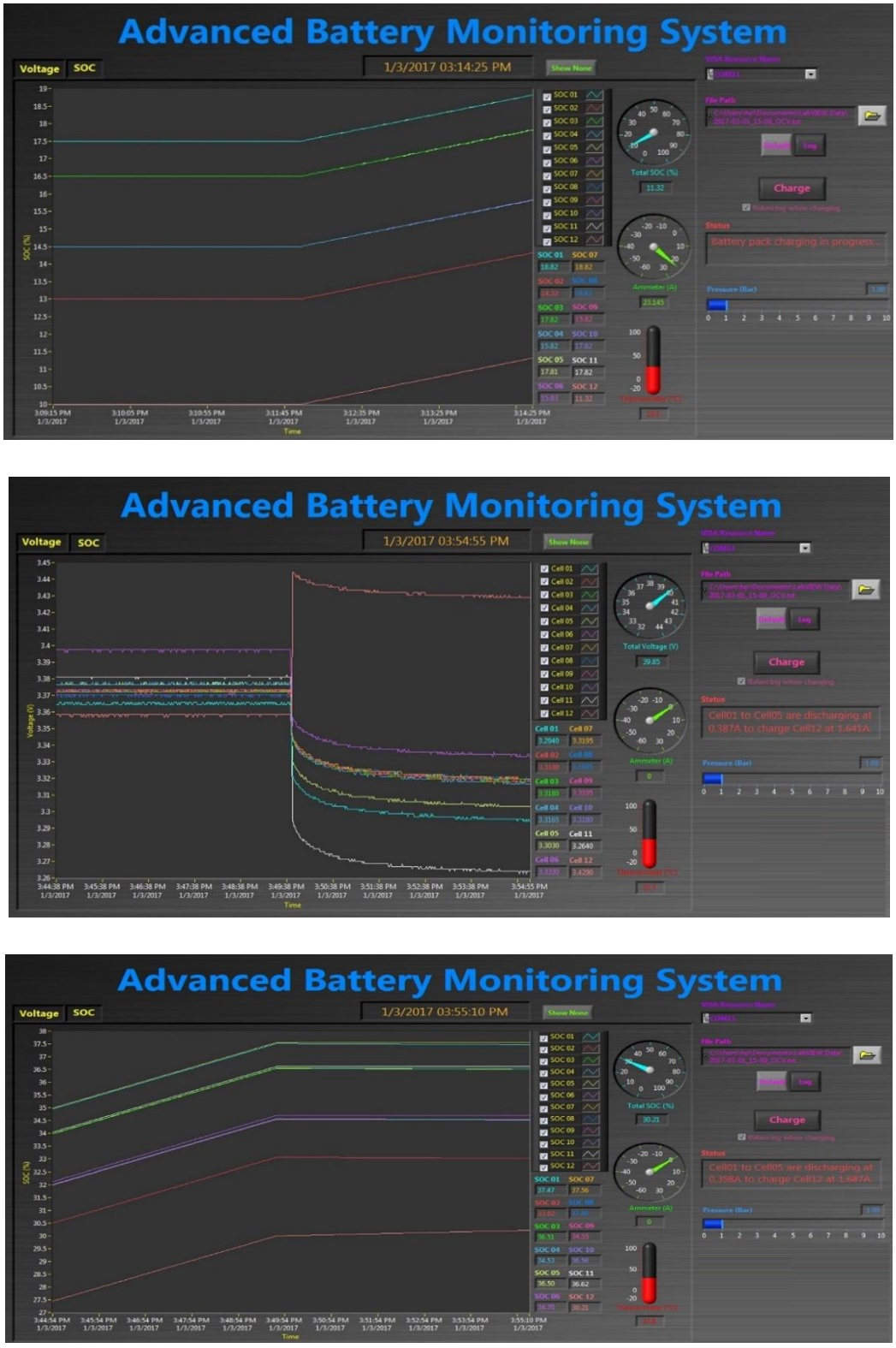

Figure 12: LabVIEW GUI (a) initial SOC of cells; (b) voltage tab for charging battery pack;(c) SOC tab for charging battery pack; (d) voltage tab after active balancing; (e) SOC tab after active balancing

6. Conclusions

The battery power system for the offshore industry is a mechatronics system. The battery power system had gone through multiple design iterations to reach the final hardware, software, and interfacing design. The battery modeling, simulation, and experimental validation were conducted to test the functionality and reliability of the system in water before future implementation in remotely-operated vehicle (ROV). Due to the subsea temperatures, the thermal characteristic of the battery cells in the enclosure at low temperatures was investigated using COMSOL.

The results showed that the operating temperature was within the specification of the battery cell of 50 °C. The smart battery management system (BMS) could perform active cell balancing and state of charge (SOC) estimation in real-time. The experimental test successfully validated the capability of SOC estimation and active cell balancing in water. The average variation of SOC for the 12-cell was around 5%. The smart BMS was capable to estimate SOC and perform the active cell balancing under the imbalanced SOC values of at least 30 %.

For future works, the battery power system will be installed and tested on an actual ROV used for the offshore industry.

Conflicts of Interests

None.

Acknowledgments

The work presented herewith has been funded by the Singapore Maritime Institute under Maritime Energy Systems (MES) R&D Programme (ID: SMI-2013-MA-05) with Temasek Polytechnic and Soil Machine Dynamics Ltd in Singapore. We would like to thank Mr Chris Winkiston and Dr. Mahesh Menon for their support during the project.

Nomenclature

t_w	wall thickness of cylinder	m
x	axial coordinates	m
r	radial coordinate	m
P	pressure acting on cylinder	Pa (N/m^2)
t_f	thickness of flat end	m
d	inner diameter	m
S	maximum allowable stress	Pa (N/m^2)
R_I	inner radius of cylinder wall	m
R_O	outer radius of cylinder wall	m
Q_{Joule}	Joule heating effect	J
I	discharging current	A
R_i	internal resistance of the battery	Ω
C_P	heat capacity at constant pressure	J/kgK
T	temperature	K
u	velocity field	m/s
k	thermal conductivity	W/mK
Q	heat source	W/m^3
p	fluid pressure	Pa (N/m^2)
F	volume force field	N/m^3
C_1 *and* C_2	capacitors of battery	F
R_0, R_1 *and* R_2	resistances of battery	Ω
R_i	total internal resistance	Ω

$a, b, c, d \text{ and } f$	coefficients of curve fitting	-
t_d	pulse discharge duration	s
$V_{OC(charge)}$	open-circuit voltage during charging	V
$V_{OC(discharge)}$	open-circuit voltage during discharging	V
V_t	terminal voltage	V
C_{max}	maximal releasable capacity	F
C_{rated}	rated capacity	F

Greek letters

θ	angular coordinate	degree
σ_θ	stress in the circumference called hoop stress	Pa (N/m^2)
σ_x	stress along the axial direction called longitudinal stress	Pa (N/m^2)
μ	fluid dynamic viscosity	Pa.s
ρ	density	kg/m^3

Subscripts and superscripts

w	wall
f	flat end head or cap
d	discharging
θ	circumference direction
x	axial direction
i	internal
I	inner
p	constant pressure
oc	open-circuit
1	first component

2	second component
t	terminal
max	maximum value
rated	rated value
amb	ambient

Abbreviations

BP	British Petroleum
URV	underwater robotic vehicles
ROV	remotely-operated vehicle
AUV	autonomous vehicle
SOC	state-of-charge
DC	Direct current
AC	Alternating current
3D	three-dimensional
CAD	computer-aided design
PCM	phase change material
PCB	printed circuit board
SOH	state-of-health
BMS	battery management system
CCCV	constant current-constant voltage
OCV	open circuit voltage
GUI	graphical user interface
MCU	microcontroller
PEC	packet error check
ID	Identification

7. References

[1]British Petroleum, Report on causes of Gulf of Mexico tragedy, https://www.bp.com/en/global/corporate/news-and-insights/press-releases/bp-releases-report-on-causes-of-gulf-of-mexico-tragedy.html, 2010 (accessed 22 December 2018).

[2] J. Han, J.F. Charpentier, T. Tang, An energy management system of a fuel cell/battery hybrid boat, Energies, 7(5) (2014) 2799-2820. https://doi.org/10.3390/en7052799.

[3] K. Kim, K. Park, J. Ahn, G. Roh, K. Chun, A study on applicability of battery energy storage system (BESS) for electric propulsion ships. 2016 IEEE Transportation Electrification Conference and Expo, Asia-Pacific, (2016) 203-207. https://doi.org/10.1109/ITEC-AP.2016.7512948

[4] T. I. Bø, T.A. Johansen. Battery power smoothing control in a marine electric power plant using nonlinear model predictive control, IEEE Transactions on Control Systems Technology, 25(4) (2017) 1449 – 1456. https://doi.org/10.1109/TCST.2016.2601301

[5]Ø. Hasvold, N.J. Størkersen, S.Forseth, T. Lian. Power sources for autonomous underwater vehicles, Journal of Power Sources, 162 (2006) 935–942. https://doi.org/10.1016/j.jpowsour.2005.07.021

[6]F. Díaz-González, A. Sumper, O. Gomis-Bellmunt, R. Villafáfila-Robles. A review of energy storage technologies for wind power applications. Renewable and Sustainable Energy Reviews, 16(4) (2012) 2154-2171. https://doi.org/10.1016/j.rser.2012.01.029

[7] W.D. Toh, B. Xu, J. Jia, C.S. Chin, J. Chiew, Z. Gao. Lithium Iron Phosphate (LiFePO4) battery power system for deepwater emergency operation. Energy Procedia, 143 (2017) 348–353. https://doi.org/10.1016/j.egypro.2017.12.695

[8]S. Zhang, Y.Luo, J. Wang, X.Wang, K. Li, Predictive energy management strategy for fully electric vehicles based on preceding vehicle movement, IEEE Transactions on Intelligent Transportation Systems, 18(11) (2017) 3049-3060. https://doi.org/10.1109/TITS.2017.2672542

[9]A.A. Hussein, Capacity fade estimation in electric vehicle li-ion batteries using artificial neural networks, IEEE Transactions on Industry Applications, 51(3) (2015) 2321-2330. https://doi.org/10.1109/TIA.2014.2365152

[10] D. Tenfen, E.C. Finardi, B. Delinchant, F. Wurtz, Lithium-ion battery modeling for the energy management problem of microgrids, IET Generation, Transmission & Distribution, 10(3) (2016) 576-584. https://doi.org/10.1049/iet-gtd.2015.0423

[11] F. Ye, Y. Qian, R. Q. Hu, Incentive load scheduling schemes for PHEV battery exchange stations in smart grid, IEEE Systems Journal, 11(2) (2015) 922-930. https://doi.org/10.1109/JSYST.2015.2421642

[12]L.C. Casals, B. A. Garca, Communications concerns for reused electric vehicle batteries in smart grids, IEEE Communications Magazine, 54(9) (2016) 120-125. https://doi.org/10.1109/MCOM.2016.7565258

[13] Y.F. Wang, J.T. Wu, Performance improvement of thermal management system of lithium-ion battery module on purely electric AUVs, Applied Thermal Engineering, 146 (2019), 74-84. https://doi.org/10.1016/j.applthermaleng.2018.09.108

[14] Z.Y. Mao, S.K. Yan, Design and analysis of the thermal-stress coupled topology optimization of the battery rack in an AUV, Ocean Engineering, 148 (2018) 401-411. https://doi.org/10.1016/j.oceaneng.2017.11.025

[15] G.L. Plett, Extended Kalman filtering for battery management systems of LiPB-based HEV battery packs: Part 2. Modeling and identification. J. Power Sources, 134 (2004) 262-276. https://doi.org/10.1016/j.jpowsour.2004.02.032

[16] M. Cacciato, G. Nobile, G. Scarcella, G. Scelba, Real-time model-based estimation of SOC and SOH for energy storage systems, IEEE Transactions on Power Electronics, 32(1) (2017) 794-803. https://doi.org/10.1109/TPEL.2016.2535321

[17] S. Panchal, I. Dincer, M. Agelin-Chaab, R. Fraser, M. Fowler, Experimental and simulated temperature variations in a $LiFePO_4$-20Ah battery during discharge process, Applied Energy, 180 (2016), 504-515. https://doi.org/10.1016/j.apenergy.2016.08.008

[18] S. Panchal, S. Mathewson, R. Fraser, R. Culham, M. Fowler, Experimental Measurements of Thermal Characteristics of $LiFePO_4$ Battery, SAE Technical Paper, 2015-01-1189 (2015) https://doi.org/10.4271/2015-01-1189.

[19] L.H. Saw, Y. H. Ye, A.A.O. Tay, Electrochemical–thermal analysis of 18650 Lithium Iron Phosphate cell, Energy Conversion and Management, 75 (2013) 162–174. https://doi.org/10.1016/j.enconman.2013.05.040

[20] L. Cai, R. E. White, Mathematical modeling of a lithium ion battery with thermal effects in COMSOL Inc. Multiphysics (MP) software. Journal of Power Source, 196 (2011) 5985-5989. https://doi.org/10.1016/j.jpowsour.2011.03.017

[21] J. Chiew, C.S. Chin, J. Jia, W.D. Toh, Thermal analysis of a latent heat storage based battery thermal cooling wrap, COMSOL Conference, Singapore, 2017. https://www.comsol.com/paper/download/504332/tan_paper.pdf

[22] J. Chiew, C.S. Chin, J.B. Jia, W.D. Toh, Thermal Analysis of a Sealed Battery Power System Enclosure for Underwater Operations, 2015 COMSOL Conference, Kuala Lumpur, Malaysia, 2015. https://www.comsol.com/paper/download/299891/joel_paper.pdf

[23] L.H. Saw, Y. Ye, A.A.O. Tay, Feasibility study of Boron Nitride coating on Lithium-ion battery casing, Applied Thermal Engineering 73 (2014) 154-161. https://doi.org/10.1016/j.applthermaleng.2014.06.061

[24] Y. Ye, Y. Shi, L. H. Saw, A. A.O.Tay, Simulation and evaluation of capacity recovery methods for spiral-wound lithium ion batteries, Journal of Power Sources, 243 (2013), 779-789. https://doi.org/10.1016/j.jpowsour.2013.06.083

[25] Z. Li, J. Huang , B. Y. Liaw , J. Zhang, On state-of-charge determination for lithium-ion batteries, Journal of Power Sources, 348 (2017) 281-301. https://doi.org/10.1016/j.jpowsour.2017.03.001

[26] J. Jaguemont , L. Boulon, Y. Dubé, A comprehensive review of lithium-ion batteries used in hybrid and electric vehicles at cold temperatures, Applied Energy, 164 (2016) 99-114. https://doi.org/10.1016/j.apenergy.2015.11.034

[27] A. Marongiu, F. G. W. Nußbaum, W. Waag, M.Garmendi, D. U. Sauer, Comprehensive study of the influence of aging on the hysteresis behavior of a lithium iron phosphate cathode-based lithium ion battery – An experimental investigation of the hysteresis, Applied Energy, 171 (2016) 629-645. https://doi.org/10.1016/j.apenergy.2016.02.086

[28] M.A. Hannan, M.S.H. Lipu, A. Hussain, A. Mohamed. A review of lithium-ion battery state of charge estimation and management system in electric vehicle applications: Challenges and

recommendations, Renewable and Sustainable Energy Reviews, 78 (2017) 834-854. https://doi.org/10.1016/j.rser.2017.05.001

[29] W. Waag, C. Fleischer, D.U. Sauer, Critical review of the methods for monitoring of lithium-ion batteries in electric and hybrid vehicles, Journal of Power Sources 258 (2014) 321-339. https://doi.org/10.1016/j.jpowsour.2014.02.064

[30] General Dynamics Mission Systems Inc., Bluefin 1.5 kWh Subsea Battery, https://gdmissionsystems.com/en/products/underwater-vehicles/bluefin-robotics/1-5-kwh-subsea-battery, 2018 (accessed 22 December 2018).

[31] Ashtead Technology Inc., CDL Subsea Battery Pack, https://www.ashtead-technology.com/rental-equipment/cdl-subsea-battery-pack/, 2018. (accessed 22 December 2018).

[32]Southwest Electronic Energy Group, SWE SeaSafe Subsea Battery Modules, https://www.swe.com/seasafe-subsea-modules/, 2018. (accessed 22 December 2018).

[33]Seatronics Group, Sea Battery Power Light Module, https://seatronics-group.com/files/6114/1811/8353/DeepSea_Power__Light_SeaBattery_-_Datasheet.pdf, 2018 (accessed 22 December 2018).

[34] Furukawa Battery Company of Japan, Eco Marine Power, https://www.furukawadenchi.co.jp/english/products/indust/ub.htm , 2018 (accessed 22 December 2018).

[35] PlanB E Storage Ltd, PBES Specification Sheet, http://www.pbes.com/wp-content/uploads/2018/07/PBES-Overview-NMC-LTO_2018-07-11.pdf, 2018 (accessed 22 December 2018).

[36] J. Lee, in Electrochemical and Thermal Modeling of Battery, Fuel cell, and Photoenergy Conversion Systems, J. R. Selman and H. C. Maru, Editors, PV 86-12, 206, The Electrochemical Society Proceedings Series, Pennington, NJ (1986).

[37] J. Newman, W. Tiedemann, Temperature Rise in a Battery Module with Constant Heat Generation, J. Electrochem. Soc., 142(4) (1995) 1054-1057. https://doi.org/10.1149/1.2044130.

[38] M.S. Rad, D. L. Danilov, M. Baghalha, M. Kazemeini, P. H. L. Notten, Thermal modeling of cylindrical LiFePO4 batteries, Journal of Modern Physics, 4 (2013) 1-7. http://dx.doi.org/10.4236/jmp.2013.47A2001